JOINT SPECTRAL SUBSPACE AND ABUNDANCE ESTIMATION WITH UNTRAINED NEURAL NETWORK PRIORS FOR MS-HS FUSION

Dan Pineau[1, 2, 4], Françcois Orieux[2], Alain Abergel[3, 4]

ABSTRACT

Multispectral and hyperspectral (MS-HS) data fusion aims to reconstruct data with both high spatial and spectral resolutions from complementary degraded observations. This work addresses the fusion of high-dimensional infrared data affected by spectrally varying spatial blurs when the spectral subspace is unknown. We propose to adapt Untrained Neural Network Prior (UNNP) architectures to jointly estimate abundance maps and their associated spectra within a low-rank model, avoiding a preliminary spectral unmixing step from degraded hyperspectral data. The spectra are represented by an additional set of optimizable parameters, while the abundance maps are generated by the untrained networks. Convergence instability and noise overfitting are mitigated using an automatic residual-based stopping criterion and a reused dropout-based architecture. Experiments on simulated realistic data inspired by the Mid-Infrared Instrument of the James Webb Space Telescope show that jointly estimating spectra and abundance maps improves reconstruction quality compared with split NMF-based approaches and full-cube UNNP reconstruction, while preserving the dimensionality reduction benefits of the low-rank model.

***Index Terms*—** Data fusion, hyperspectral, untrained neural network, low-rank, joint optimization

1. INTRODUCTION

Multispectral and hyperspectral (MS-HS) fusion aims to reconstruct a datacube with both high spatial and spectral resolutions by combining high-spatial/low-spectral MS data with low-spatial/high-spectral HS data [1]. This work focuses on the high-dimensional case with spectrally varying spatial blurs, as encountered in infrared astronomical imaging, where the instrumental point spread function varies strongly with wavelength. MIRI/JWST provides a representative example, combining imaging and spectroscopic modes over the mid-infrared range [2].

[1] AIRMO S.à.r.l., Esch-sur-Alzette, Luxembourg
[2] Université Paris-Saclay, CNRS, CentraleSupélec, Laboratoire des Signaux et Systèmes, 3 rue Joliot Curie, 91190 Gif-sur-Yvette, France
[3] Institut d'Astrophysique Spatiale (IAS), CNRS, UMR 8617, Université Paris-Saclay, 91405 Orsay, France
[4] Innovative Common Laboratory For Space Spectroscopy (INCLASS), IAS, ACRI-ST, CNRS, Université Paris-Saclay, 91405 Orsay, France
Part of this work was supported by the Centre National d'Études Spatiales (CNES) and the French National Research Agency (ANR).

Model-based methods address this problem by minimizing data-fidelity terms combined with handcrafted regularization, while explicitly using the instrument forward models [3, 4, 5]. Although interpretable and effective, such priors have limited discriminative power in highly ill-posed settings and may oversmooth the reconstruction or amplify artifacts in noisy observations [6].

Deep learning methods can learn powerful image priors for inverse problems [7], but their use in astronomical MS-HS fusion is limited by the scarcity of representative training data. Simulated datasets can be used, but performance then depends strongly on simulation realism and may not generalize to real observations.

Untrained Neural Network Priors (UNNPs) use the neural architecture itself as an implicit prior and therefore avoid supervised pretraining [8]. They have been applied to MS-HS fusion through approaches such as GDD [9] and DeepSURE [10], but these methods do not account for spectrally varying spatial blurs and reconstruct the full hyperspectral datacube directly. This can become computationally demanding for high-dimensional astronomical data. Our previous work [11] addressed spectrally varying blurs and high-dimensional reconstruction by combining a compact Deep Decoder [12] with a low-rank linear mixing model, reconstructing abundance maps rather than the full cube. However, it assumed the spectral subspace to be known and used a compact architecture whose expressiveness and robustness to optimization instability remained limited.

In this paper, we address the more realistic case where the spectral subspace is unknown. Our contributions are threefold. First, we extend low-rank UNNP-based MS-HS fusion by jointly estimating the abundance maps and their associated spectra, avoiding a preliminary spectral unmixing step. Second, we adapt several UNNP architectures to MS-HS fusion with spectrally varying spatial blurs, including a dropout-based variant inspired by [13] and a residual-based stopping criterion to improve optimization stability and reduce noise overfitting. Third, experiments on realistic MIRI/JWST simulations show that the proposed joint estimation strategy improves reconstruction quality over split NMF-based approaches and full-cube UNNP reconstructions.

2. MODELS DESCRIPTION

2.1. Low-rank spectral model

Let $\boldsymbol{x}$ denote the hyperspectral datacube to reconstruct, with spatial size $I \times J$ and L wavelength samples, and let $\boldsymbol{x}_l \in \mathbb{R}^{I\times J}$ be its image at wavelength l. To reduce the number of unknowns, we use a linear mixing model, as commonly done in MS-HS fusion [14, 3, 15]:

$$\boldsymbol{x}[i,j,l] = \sum_{t=1}^{T} \boldsymbol{a}_t[i,j]\, \boldsymbol{s}_t[l], \tag{1}$$

where $\boldsymbol{s}_t$ is the t-th spectrum and $\boldsymbol{a}_t$ its associated abundance map. Unlike in our previous works [4, 11, 5], the spectra $\boldsymbol{s}_t{}_{t=1}^{T}$ are unknown and estimated jointly with the abundance maps. In vectorized form, the model is written as

$$\boldsymbol{x} = \boldsymbol{T}\boldsymbol{a}, \tag{2}$$

where $\boldsymbol{T}$ denotes the spectral subspace induced by the spectra $\{\boldsymbol{s}_t\}_{t=1}^{T}$, and $\boldsymbol{a}$ is the vectorized set of abundance maps. This representation reduces the number of spatial unknowns from LIJ to TIJ, with $T \ll L$, while preserving spectral correlations through $\boldsymbol{T}$.

2.2. Multispectral data formation process

The multispectral observation $\boldsymbol{y}_{\mathrm{m}}$ is composed of C wideband images obtained by wavelength-dependent spatial blurring, spectral weighting, and integration over wavelength. For channel c,

$$\boldsymbol{y}_{\mathrm{m}}^{c}[i,j] = \sum_{l=1}^{L} \left(\boldsymbol{x}_l \underset{i,j}{*} \boldsymbol{h}_{\mathrm{m},l}^{c} \right)[i,j]\, \boldsymbol{w}_{\mathrm{m}}^{c}[l] + \boldsymbol{n}_{\mathrm{m}}^{c}[i,j], \tag{3}$$

where $\boldsymbol{h}_{\mathrm{m},l}^{c}$ is the point spread function, $\underset{i,j}{*}$ denotes the two-dimensional spatial convolution, $\boldsymbol{w}_{\mathrm{m}}^{c}[l]$ is the spectral response of the c-th channel at wavelength l, and $\boldsymbol{n}_{\mathrm{m}}^{c}$ is additive white Gaussian noise with standard deviation σ_{m}. After vectorization and channel concatenation,

$$\boldsymbol{y}_{\mathrm{m}} = \boldsymbol{M}\boldsymbol{x} + \boldsymbol{n}_{\mathrm{m}}, \tag{4}$$

where $\boldsymbol{M}$ gathers the spatial blurs, spectral responses, and spectral integrations, and where $\boldsymbol{x}$ can be estimated using the low-rank model (2).

2.3. Hyperspectral data formation process

The hyperspectral observation $\boldsymbol{y}_{\mathrm{h}}$ provides finer spectral sampling at lower spatial resolution. For spectrometer k, the model includes wavelength-dependent blur, spectral response, and spatial downsampling represented as an integration over blocks of $d_i \times d_j$ high-resolution pixels. Denoting by $\mathcal{B}_{\bar{i},\bar{j}}$ the set of high-resolution pixels contributing to the low-resolution pixel $(\bar{i},\bar{j})$, the hyperspectral data are written as

$$\boldsymbol{y}_{\mathrm{h}}^{k}[\bar{i},\bar{j},l] = \sum_{(i,j)\in\mathcal{B}_{\bar{i},\bar{j}}} \left(\boldsymbol{x}_l \underset{i,j}{*} \boldsymbol{h}_{\mathrm{h},l}^{k} \right)[i,j]\, \boldsymbol{w}_{\mathrm{h}}^{k}[l] + \boldsymbol{n}_{\mathrm{h}}^{k}[\bar{i},\bar{j},l], \tag{5}$$

where $\boldsymbol{n}_{\mathrm{h}}^{k}$ is additive white Gaussian noise with standard deviation σ_{h}. After vectorization and concatenation,

$$\boldsymbol{y}_{\mathrm{h}} = \boldsymbol{H}\boldsymbol{x} + \boldsymbol{n}_{\mathrm{h}}, \tag{6}$$

where $\boldsymbol{H}$ gathers the spectrally varying spatial blurs, spectral responses, and spatial integrations, where $\boldsymbol{x}$ can be estimated using the low-rank model (2). Equations (4) and (6) define the forward models used in the following section.

3. METHODOLOGY

3.1. Joint estimation of abundance maps and spectra

The fusion problem considered in this paper is solved with a joint approach: both the abundance maps $\boldsymbol{a}$ and their associated spectral subspace $\boldsymbol{T}$ are estimated from the observed MS and HS data. The abundance maps are generated by an untrained neural network with parameters $\boldsymbol{\theta}$, while the spectral subspace is directly parameterized by an additional variable $\boldsymbol{\varphi}$, independent of $\boldsymbol{\theta}$. We denote these quantities by $\boldsymbol{a}(\boldsymbol{\theta})$ and $\boldsymbol{T}(\boldsymbol{\varphi})$, where $\boldsymbol{\varphi}$ has the same dimension as the spectral subspace. The output of f is

$$f(\boldsymbol{\theta},\boldsymbol{\varphi}) = \boldsymbol{T}(\boldsymbol{\varphi})\boldsymbol{a}(\boldsymbol{\theta}) \tag{7}$$

where $f(\boldsymbol{\theta},\boldsymbol{\varphi})$ is a hyperspectral datacube. For the non-stochastic architectures used in this paper, $\boldsymbol{\theta}$ and $\boldsymbol{\varphi}$ are estimated by minimizing the data-fidelity criterion

$$\begin{aligned} \mathcal{L}(\boldsymbol{\theta},\boldsymbol{\varphi}) =& \mu_{\mathrm{m}} \left\| \boldsymbol{y}_{\mathrm{m}} - \boldsymbol{M} f(\boldsymbol{\theta},\boldsymbol{\varphi}) \right\|_2^2 \\ &+ \mu_{\mathrm{h}} \left\| \boldsymbol{y}_{\mathrm{h}} - \boldsymbol{H} f(\boldsymbol{\theta},\boldsymbol{\varphi}) \right\|_2^2, \end{aligned} \tag{8}$$

where $\mu_{\mathrm{m}} = 1/(2\sigma_{\mathrm{m}}^2)$ and $\mu_{\mathrm{h}} = 1/(2\sigma_{\mathrm{h}}^2)$. No handcrafted regularization term is added; regularization is induced by the network architecture and, when used, by stochastic procedures.

3.2. Adapted UNNP architectures

Three UNNP architectures, originally built for the reconstruction of RGB images or full hyperspectral cubes, are adapted to the present fusion problem by changing the output dimension to reconstruct T abundance maps and by jointly optimizing the spectral parameters $\boldsymbol{\varphi}$.

DD-SE is inspired by the Deep Decoder [12] and maps a fixed random tensor to abundance maps $\boldsymbol{a}_{\mathrm{DD}}(\boldsymbol{\theta})$. GDD-SE is inspired by the Guided Deep Decoder [9] and additionally uses guidance data $\boldsymbol{G}$, chosen here as the MS observation

$\boldsymbol{G} = \boldsymbol{y}_{\mathrm{m}}$. Their reconstructed datacubes are

$$f_{\mathrm{DD}}(\boldsymbol{\theta}, \boldsymbol{\varphi}) = \boldsymbol{T}(\boldsymbol{\varphi})\boldsymbol{a}_{\mathrm{DD}}(\boldsymbol{\theta}), \tag{9}$$

$$f_{\mathrm{GDD}}(\boldsymbol{G}, \boldsymbol{\theta}, \boldsymbol{\varphi}) = \boldsymbol{T}(\boldsymbol{\varphi})\boldsymbol{a}_{\mathrm{GDD}}(\boldsymbol{G}, \boldsymbol{\theta}). \tag{10}$$

SAD-SE is inspired by the dropout-based untrained network of Chen *et. al.* [13]. We remove the final sigmoid activation to avoid excessively constraining the abundance maps and add batch-normalization layers to improve optimization stability.

We retain the main stochastic mechanisms of Chen *et. al.* [13], adapted to MS-HS fusion. At iteration q, dropout is applied to the network parameters, yielding dropped parameters $\boldsymbol{\theta}_{\delta}^{(q)}$. At the same iteration, the input of the network $\boldsymbol{y}_{\mathrm{in}}^{(q)}$ is chosen as a randomly modified version of the MS data $\boldsymbol{y}_{\mathrm{m}}$ by replacing a subset of pixels $\boldsymbol{\omega}^{(q)}$ by local spatial averages. The same spatial mask is applied to all MS channels to preserve spectral consistency.

The SAD-SE loss differs from the generic criterion (8) by evaluating the MS residual only on the modified pixels, while keeping the full HS residual:

$$\begin{aligned}\mathcal{L}_{\mathrm{SAD}}^{(q)}(\boldsymbol{\theta}, \boldsymbol{\varphi}) =& \mu_{\mathrm{m}} \left\| \boldsymbol{\omega}^{(q)} \odot \left[\boldsymbol{y}_{\mathrm{m}} - \boldsymbol{M} f_{\mathrm{SAD}} \left(\boldsymbol{y}_{\mathrm{in}}^{(q)}, \boldsymbol{\theta}_{\delta}^{(q)}, \boldsymbol{\varphi} \right) \right] \right\|_2^2 \\ &+ \mu_{\mathrm{h}} \left\| \boldsymbol{y}_{\mathrm{h}} - \boldsymbol{H} f_{\mathrm{SAD}} \left(\boldsymbol{y}_{\mathrm{in}}^{(q)}, \boldsymbol{\theta}_{\delta}^{(q)}, \boldsymbol{\varphi} \right) \right\|_2^2 .\end{aligned} \tag{11}$$

This masked criterion prevents the network from simply reproducing the MS input and contributes to limiting noise overfitting.

After optimization, the parameters $\widehat{\boldsymbol{\theta}}$ and $\widehat{\boldsymbol{\varphi}}$ are fixed, and the final reconstructed datacube is obtained by averaging N_{avg} stochastic outputs with dropout and input masking still activated, as

$$\widehat{\boldsymbol{x}} = \frac{1}{N_{\mathrm{avg}}} \sum_{r=1}^{N_{\mathrm{avg}}} f_{\mathrm{SAD}} \left(\boldsymbol{y}_{\mathrm{in}}^{(r)}, \widehat{\boldsymbol{\theta}}_{\delta}^{(r)}, \widehat{\boldsymbol{\varphi}} \right). \tag{12}$$

3.3. Stopping criterion

UNNPs are known to be sensitive to noise overfitting when optimized for too many iterations. Since the ground truth is unavailable in real applications, the stopping rule cannot rely on reconstruction metrics such as PSNR. We therefore use a criterion based on the normalized residuals with respect to both observations as

$$\rho(\boldsymbol{x}) = \frac{1}{2\sigma_{\mathrm{m}}^2} \left\| \boldsymbol{y}_{\mathrm{m}} - \boldsymbol{M}\boldsymbol{x} \right\|_2^2 + \frac{1}{2\sigma_{\mathrm{h}}^2} \left\| \boldsymbol{y}_{\mathrm{h}} - \boldsymbol{H}\boldsymbol{x} \right\|_2^2 . \tag{13}$$

The stopping criterion is motivated by the fact that, once the reconstruction fits the observations up to the noise level, the residuals should satisfy

$$\left\| \boldsymbol{y}_{\mathrm{m}} - \boldsymbol{M}\boldsymbol{x} \right\|_2^2 \simeq \left\| \boldsymbol{n}_{\mathrm{m}} \right\|_2^2 , \tag{14}$$

$$\left\| \boldsymbol{y}_{\mathrm{h}} - \boldsymbol{H}\boldsymbol{x} \right\|_2^2 \simeq \left\| \boldsymbol{n}_{\mathrm{h}} \right\|_2^2 \tag{15}$$

assuming the residual norms are normalized by the number of measurements. The optimization is therefore stopped when

$$\rho(\boldsymbol{x}) \simeq 1. \tag{16}$$

For SAD-SE, ρ is evaluated on the averaged reconstruction from (12). This provides an unsupervised way to limit noise overfitting without requiring access to the ground truth.

4. RESULTS

4.1. Experimental setup

Experiments are conducted on realistic simulated MS and HS data inspired by MIRI/JWST. The reference hyperspectral datacube is generated from $T = 5$ abundance maps of size 128×256 and their associated spectra sampled over the MIRI spectral range. The MS and HS observations are obtained with the forward models of Section 2, with $C = 9$ (MS) and spatial integration over regions of 4×4 pixels (HS), and corrupted with additive white Gaussian noise at $\mathrm{SNR}_{\mathrm{dB}} = 30$ dB.

DD-SE, GDD-SE, and SAD-SE are compared with two baselines. The first follows a split strategy, where the spectral subspace is estimated from the HS observation using NMF before reconstructing abundance maps with model-based ℓ_2 [4] and $\ell_{2,1}$ [5] regularizations, denoted ℓ_2-NMF and $\ell_{2,1}$-NMF. The second is GDD-Cube [9], which directly reconstructs the full hyperspectral cube without low-rank factorization.

4.2. Comparison of reconstruction methods

The reconstruction results are reported in Table 1, while Fig. 1 shows the evolution of the PSNR during optimization. Figs. 2 and 3 provide visual and spectral comparisons.

The two NMF-based methods provide the lowest reconstruction quality. Although they recover the main low-frequency structures in Fig. 2, their reconstructions remain spatially oversmoothed and fail to accurately restore high-frequency details. Fig. 3 further shows that their reconstructed spectra deviate from the reference in a high-spatial-frequency region, especially at long wavelengths. This confirms the limitation of the split strategy: errors made when estimating the spectral subspace from the degraded HS data directly affect the subsequent fusion step.

Joint UNNP-based methods substantially improve the reconstruction. DD-SE reaches the best peak PSNR and NRMSE, but its convergence is unstable, with the best reconstruction obtained only over a narrow range of iterations. GDD-SE is more stable but less accurate than DD-SE and SAD-SE; nevertheless, it outperforms GDD-Cube, confirming the benefit of jointly estimating a low-rank spectral subspace and abundance maps instead of reconstructing the full cube directly.

Methods	NRMSE	PSNR [dB]	SSIM	SAM
ℓ_2 - NMF	7.47	38.58	98.86	54.26
$\ell_{2,1}$ - NMF	7.28	38.80	99.07	53.97
DD - SE	**1.78**	**51.03**	99.55	6.44
GDD - SE	2.01	49.96	99.40	**6.01**
GDD - Cube [9]	2.40	48.44	99.06	9.48
SAD - SE	1.79	51.00	**99.56**	7.27

Table 1: Comparison of reconstruction quality metrics. The best result for each column is **bold and underlined**, and the second best is underlined. Metric values, except for PSNR, were multiplied by 100 for visibility.

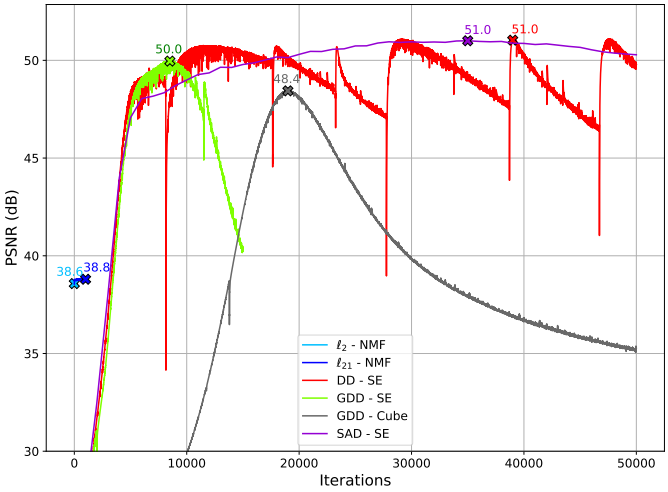


Fig. 1: PSNR of reconstruction for each method over iterations. Peak PSNR for each method is marked with a colored cross.

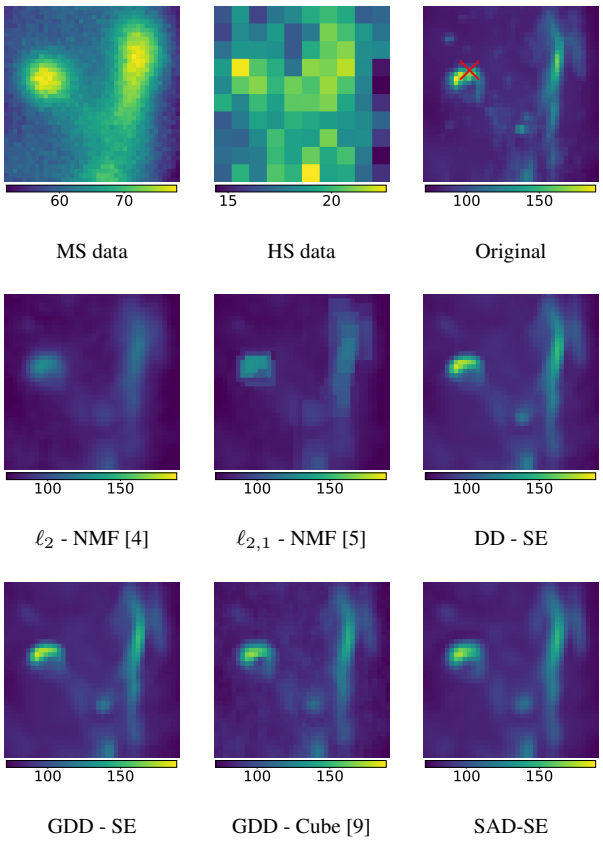


Fig. 2: Visual comparison at 25.5 μm. Top row: MS data, HS data, and reference image on the selected region. Bottom rows: reconstructions obtained with the compared methods, displayed with the same dynamic range as the reference image.

The proposed SAD-SE method provides the best compromise between reconstruction quality and optimization stability. Its quantitative results are comparable to those of DD-SE, while its convergence is more stable according to Fig. 1. Visually, SAD-SE better preserves high-frequency spatial structures than the NMF-based methods and avoids the strongest artifacts observed in some competing UNNP reconstructions. These results suggest that the combination of spatially adaptive dropout, masked data fidelity, and stochastic output averaging provides an effective implicit regularization for MS-HS fusion with unknown spectral subspace.

5. CONCLUSION

This paper addressed the MS-HS fusion problem with spectrally varying spatial blurs in the case where the spectral subspace is unknown. The main contribution was the adaptation of UNNP-based methods to jointly estimate abundance maps and their associated spectra within a low-rank model. This was achieved by introducing additional optimizable parame-

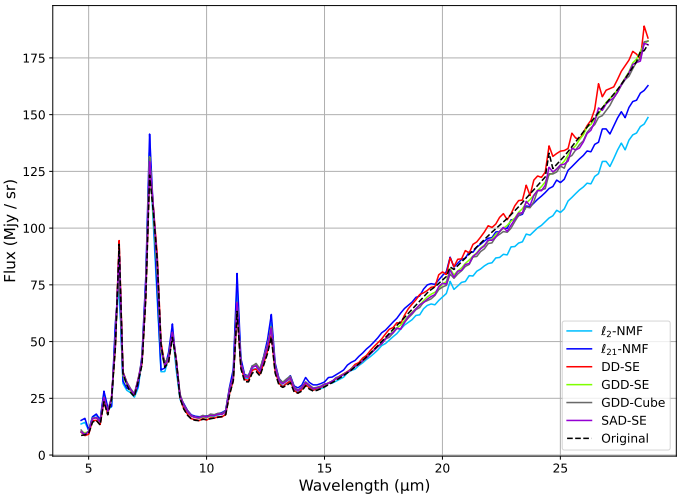


Fig. 3: Reconstructed spectra at a high spatial frequency region, shown with a red cross on the original image in Figure 2.

ters for the spectral subspace, avoiding a preliminary spectral unmixing step from the degraded HS data while preserving the dimensionality reduction benefits of the linear mixing model.

Experiments on realistic simulated MIRI/JWST data showed that joint spectral subspace and abundance estimation improves reconstruction quality over split NMF-based approaches and full-cube UNNP reconstruction. Among the tested SE methods, SAD-SE provided the best compromise between reconstruction quality and optimization stability.

The main limitation remains the computational cost, which is higher than that of classical model-based methods. In addition, excessive optimization may still cause noise overfitting, as in most UNNP-based approaches. The proposed residual-based stopping criterion offers a practical unsupervised way to limit this effect, but its robustness should be further assessed on additional datasets, instrument models, and noise configurations, including comparisons with SURE-based strategies such as DeepSURE [10].

6. REFERENCES

[1] Naoto Yokoya et al., "Hyperspectral and multispectral data fusion: A comparative review of the recent literature," *IEEE Geoscience and Remote Sensing Magazine*, vol. 5, no. 2, pp. 29–56, 2017.

[2] Gillian S Wright, George H Rieke, Alistair Glasse, Michael Ressler, Macarena García Marín, Jonathan Aguilar, Stacey Alberts, Javier Álvarez-Márquez, Ioannis Argyriou, Kimberly Banks, et al., "The mid-infrared instrument for jwst and its in-flight performance," *Publications of the Astronomical Society of the Pacific*, vol. 135, no. 1046, pp. 048003, 2023.

[3] Claire Guilloteau et al., "Hyperspectral and multispectral image fusion under spectrally varying spatial blurs–application to high dimensional infrared astronomical imaging," *IEEE Transactions on Computational Imaging*, vol. 6, pp. 1362–1374, 2020.

[4] Dan Pineau, François Orieux, and Alain Abergel, "Exact solution for multispectral and hyperspectral fusion via hessian inversion," in *Workshop on Hyperspectral Images and Signal Processing: Evolution in Remote Sensing*, 2023.

[5] Dan Pineau, François Orieux, and Alain Abergel, "Multispectral and hyperspectral image fusion with spectrally varying blurs and mm algorithm," *IEEE Transactions on Computational Imaging*, 2025.

[6] Chinmay Hegde, "Algorithmic aspects of inverse problems using generative models," in *2018 56th Annual Allerton Conference on Communication, Control, and Computing (Allerton)*. IEEE, 2018, pp. 166–172.

[7] Gregory Ongie, Ajil Jalal, Christopher A Metzler, Richard G Baraniuk, Alexandros G Dimakis, and Rebecca Willett, "Deep learning techniques for inverse problems in imaging," *IEEE Journal on Selected Areas in Information Theory*, vol. 1, no. 1, pp. 39–56, 2020.

[8] Dmitry Ulyanov, Andrea Vedaldi, and Victor Lempitsky, "Deep image prior," in *Proceedings of the IEEE conference on computer vision and pattern recognition*, 2018, pp. 9446–9454.

[9] Tatsumi Uezato, Danfeng Hong, Naoto Yokoya, and Wei He, "Guided deep decoder: Unsupervised image pair fusion," in *Computer Vision – ECCV 2020*, Andrea Vedaldi, Horst Bischof, Thomas Brox, and Jan-Michael Frahm, Eds. 2020, Lecture Notes in Computer Science, pp. 87–102, Springer International Publishing.

[10] Han V. Nguyen, Magnus O. Ulfarsson, Johannes R. Sveinsson, and Mauro Dalla Mura, "Deep SURE for unsupervised remote sensing image fusion," *IEEE Transactions on Geoscience and Remote Sensing*, vol. 60, pp. 1–13, 2022.

[11] Dan Pineau, François Orieux, and Alain Abergel, "Untrained compact neural network prior for high-dimension multispectral and hyperspectral data fusion with spectrally varying blurs," in *2024 32nd European Signal Processing Conference (EUSIPCO)*. IEEE, 2024, pp. 676–680.

[12] Reinhard Heckel and Paul Hand, "Deep decoder: Concise image representations from untrained non-convolutional networks," *arXiv preprint arXiv:1810.03982*, 2018.

[13] Mingqin Chen, Yuhui Quan, Tongyao Pang, and Hui Ji, "Nonblind image deconvolution via leveraging model uncertainty in an untrained deep neural network," *International Journal of Computer Vision*, vol. 130, no. 7, pp. 1770–1789, 2022.

[14] Mohamed Elamine Hadj-Youcef, *Spatio spectral reconstruction from low resolution multispectral data: application to the Mid-Infrared instrument of the James Webb Space Telescope*, Ph.D. thesis, Université Paris-Saclay (ComUE), 2018.

[15] Ralph Abi-Rizk et al., "Super-resolution hyperspectral reconstruction with majorization-minimization algorithm and low-rank approximation," *IEEE Transactions on Computational Imaging*, vol. 8, pp. 260–272, 2022.